

Supporting Information for

Insights into the structural features of crumpling graphene nanoribbons

Yangchao Liao †^a, Long Chen †^b, Wenjie Xia *^b

^a Department of Civil, Construction and Environmental Engineering, North Dakota State
University, Fargo, North Dakota 58108, United States

^b Department of Aerospace Engineering, Iowa State University, Ames, Iowa 50011, United
States

† These authors contributed equally to this work.

* To whom correspondence should be addressed.

Contact information: wxia@iastate.edu (W.X.)

This file includes:

Table S1

Fig. S1

Fig. S2

Fig. S3

Fig. S4

Fig. S5

Fig. S6

Fig. S7

Fig. S8

References

Table S1 Functional forms and parameters of the coarse-grained (CG) model of graphene nanoribbons (GNRs).

Interaction	Function form	Parameters
bond	$V_b(d) = D_0[1 - e^{-\alpha(d-d_0)}]^2$ for $d < d_{\text{cut}}$	$D_0 = 196.38$ kcal/mol
		$\alpha = 1.55$ Å ⁻¹
		$d_0 = 2.8$ Å
		$d_{\text{cut}} = 3.25$ Å
angle	$V_a(\theta) = k_\theta(\theta - \theta_0)^2$	$k_\theta = 409.40$ kcal/mol
		$\theta_0 = 120^\circ$
dihedral	$V_d(\phi) = k_\phi[1 - \cos(2\phi)]$	$k_\phi = 4.15$ kcal/mol
pairwise non-bonded	$V_{\text{nb}}(r) = 4\varepsilon_{\text{LJ}} \left[\left(\frac{\sigma_{\text{LJ}}}{r} \right)^{12} - \left(\frac{\sigma_{\text{LJ}}}{r} \right)^6 \right]$ for $r < r_{\text{cut}}$	$\varepsilon_{\text{LJ}} = 0.82$ kcal/mol
		$\sigma_{\text{LJ}} = 3.46$ Å
		$r_{\text{cut}} = 12$ Å

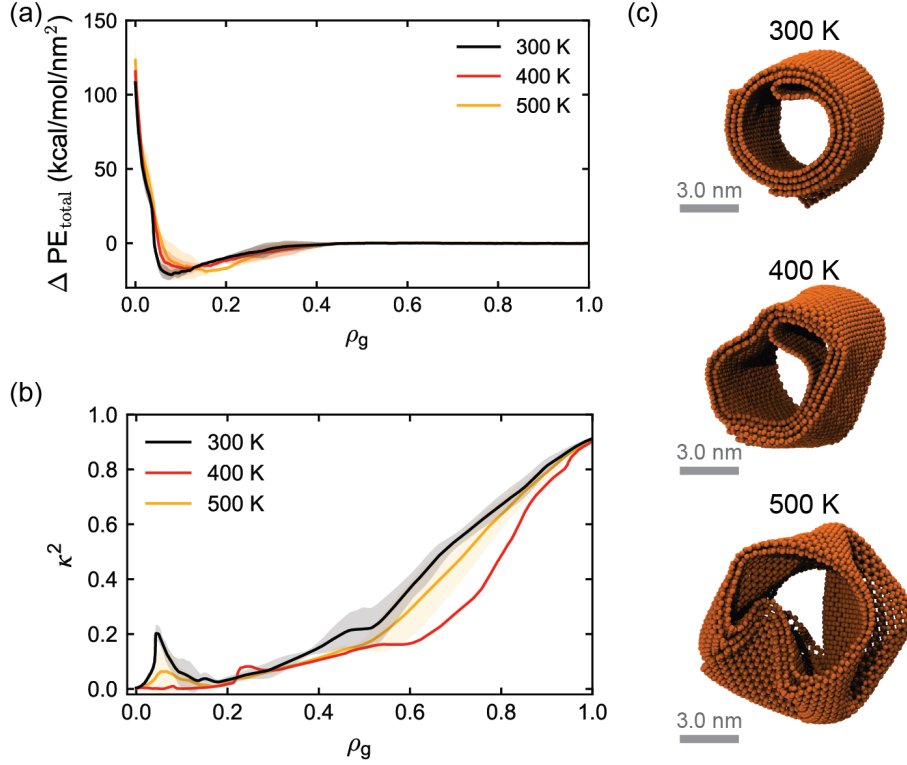


Fig. S1. Temperature effects on the crumpling behavior of GNRs with $W = 10$ and $a = 6$. (a) Evolution of the total potential energy increment ΔPE_{total} as a function of the compaction ratio ρ_g at three different temperatures (300 K, 400 K, and 500 K). (b) Evolution of relative shape anisotropy κ^2 with ρ_g . (c) Representative crumpled configurations in the QE state at different temperatures. Shaded areas of the curves correspond to the standard deviation. To assess the potential influence of thermal fluctuations — particularly for small-sized GNRs where entropic effects may be more pronounced — we performed additional simulations at elevated temperatures of 400 K and 500 K, alongside the baseline 300 K case. As shown in above figure, the evolutions of both the total potential energy increment (ΔPE_{total}) and the relative shape anisotropy (κ^2) as functions of compaction ratio (ρ_g) remain largely consistent across the three temperatures. This suggests that the overall crumpling pathway is robust with respect to thermal fluctuations. Nonetheless, the final configurations presented in Fig. S1(c) display slightly more irregular or open morphologies at higher temperatures, indicating that increased thermal agitation can enhance configurational variability. These findings suggest that while entropic effects may modulate the fine details of the final morphology, the key geometry-dependent crumpling mechanisms

identified in this study remain qualitatively valid and thermally robust within the examined temperature range.

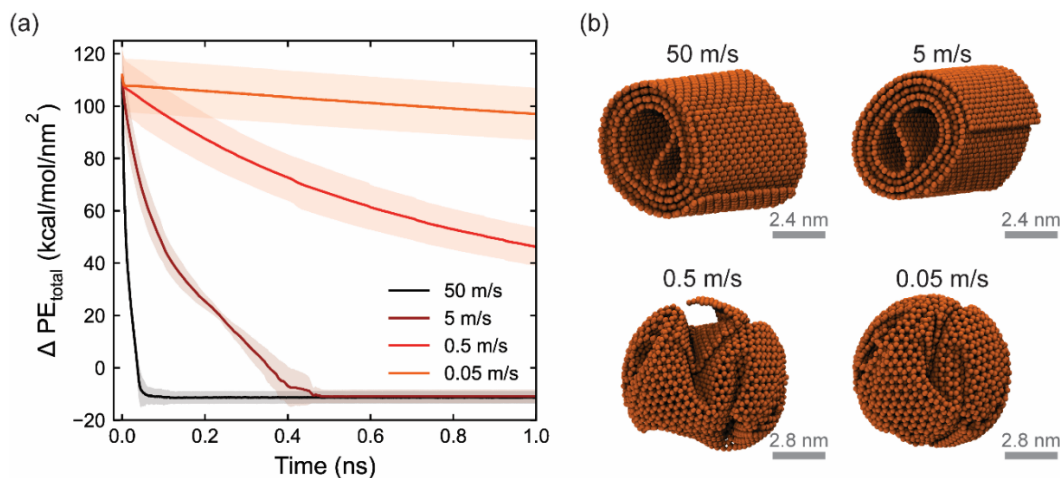


Fig. S2. Post-crumpling relaxation behavior of GNRs with $W = 10$ and $a = 6$ under different relaxation rates. (a) Time evolution of the total potential energy increment ΔPE_{total} during the relaxation process. Shaded areas of the curves correspond to the standard deviation. (b) Representative relaxed configurations at the end of the relaxation for four different relaxation rates. To assess whether crumpled GNRs retain stable mechanical properties after the confinement is removed, we performed additional simulations to analyze their post-crumpling relaxation behavior under different relaxation rates. In these simulations, GNRs with $W = 10$ nm and $a = 6$ are first crumpled to the same final confinement radius, and then gradually relaxed by removing the spherical confinement at different rates: 50 m/s, 5 m/s, 0.5 m/s, and 0.05 m/s. As shown in Fig. S2(a), the total potential energy increment (ΔPE_{total}) decreases over time in all cases, with faster relaxation rates leading to quicker stabilization. In contrast, the slowest relaxation rate (0.05 m/s) exhibits a prolonged decay in potential energy, suggesting that the structure remains far from equilibrium within the simulated timescale. The representative post-relaxation configurations in Fig. S2(b) indicate that, at a fixed short relaxation time (1 ns), faster relaxation tends to promote more ordered, scroll-like morphologies, while slower relaxation rates may result in relatively compact and disordered conformations due to kinetic trapping. However, we note that given sufficient relaxation time, even systems subjected to slow relaxation rates are expected to evolve

toward quasi-equilibrium configurations (e.g., QE state) similar to those achieved under faster relaxation, such as scroll-like laminated structures, highlighting the metastable but convergent nature of the post-crumpling states. These findings suggest that the mechanical stability and final morphology of crumpled GNRs are governed not only by relaxation rate but also by the accessible relaxation timescale, and that the quasi-equilibrium conformations identified in this study remain representative under extended post-crumpling evolution.

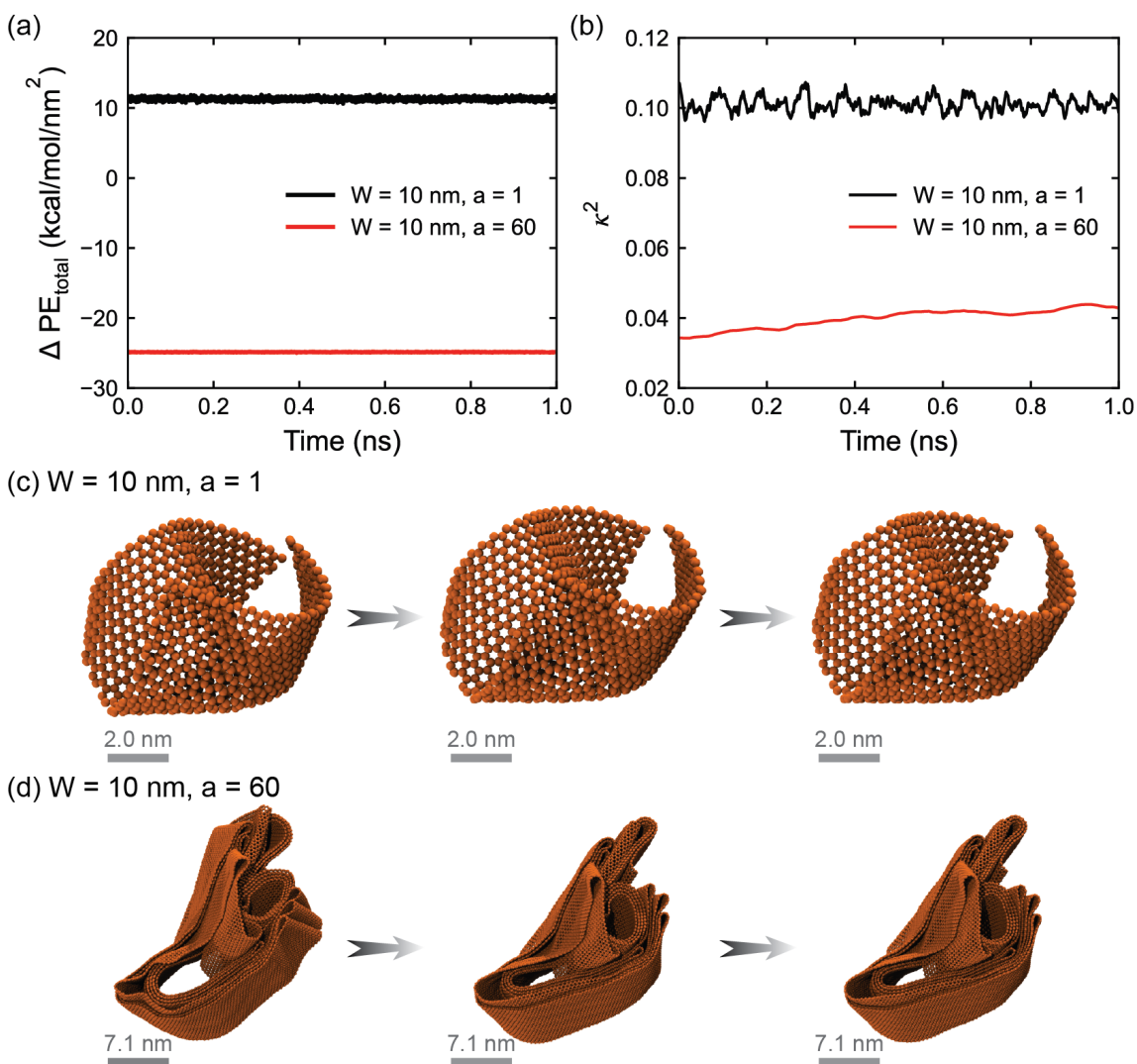


Fig. S3. Thermodynamic relaxation analysis of the crumpled GNRs in the QE state. Representative configurations of crumpled GNRs with (a) $W = 10$ nm and $a = 1$, and (b) $W = 10$ nm and $a = 60$ at different time frames over a 1 ns relaxation period after reaching the QE state. Evolution of (c) the

total potential energy increment ΔPE_{total} and (d) relative shape anisotropy κ^2 as a function of time. Here, we conducted additional relaxation simulations after the system reached the QE state. Specifically, we extended the simulations by 1 ns under the NVT ensemble, while maintaining the confining sphere radius fixed at the value corresponding to the QE state. During this period, we monitored the evolution of both the total potential energy increment (ΔPE_{total}) and the relative shape anisotropy (κ^2). As shown in above figure, both quantities remain nearly constant throughout the relaxation process, and no significant structural changes are observed in the crumpled configurations. These observations indicate that the QE state represents a mechanically stable state in which self-folding and self-adhering behaviors have largely saturated. While it may not represent a global thermodynamic equilibrium, the lack of significant energetic or morphological evolution over the extended timescale supports our assumption that the QE state corresponds to a well-relaxed, metastable configuration.

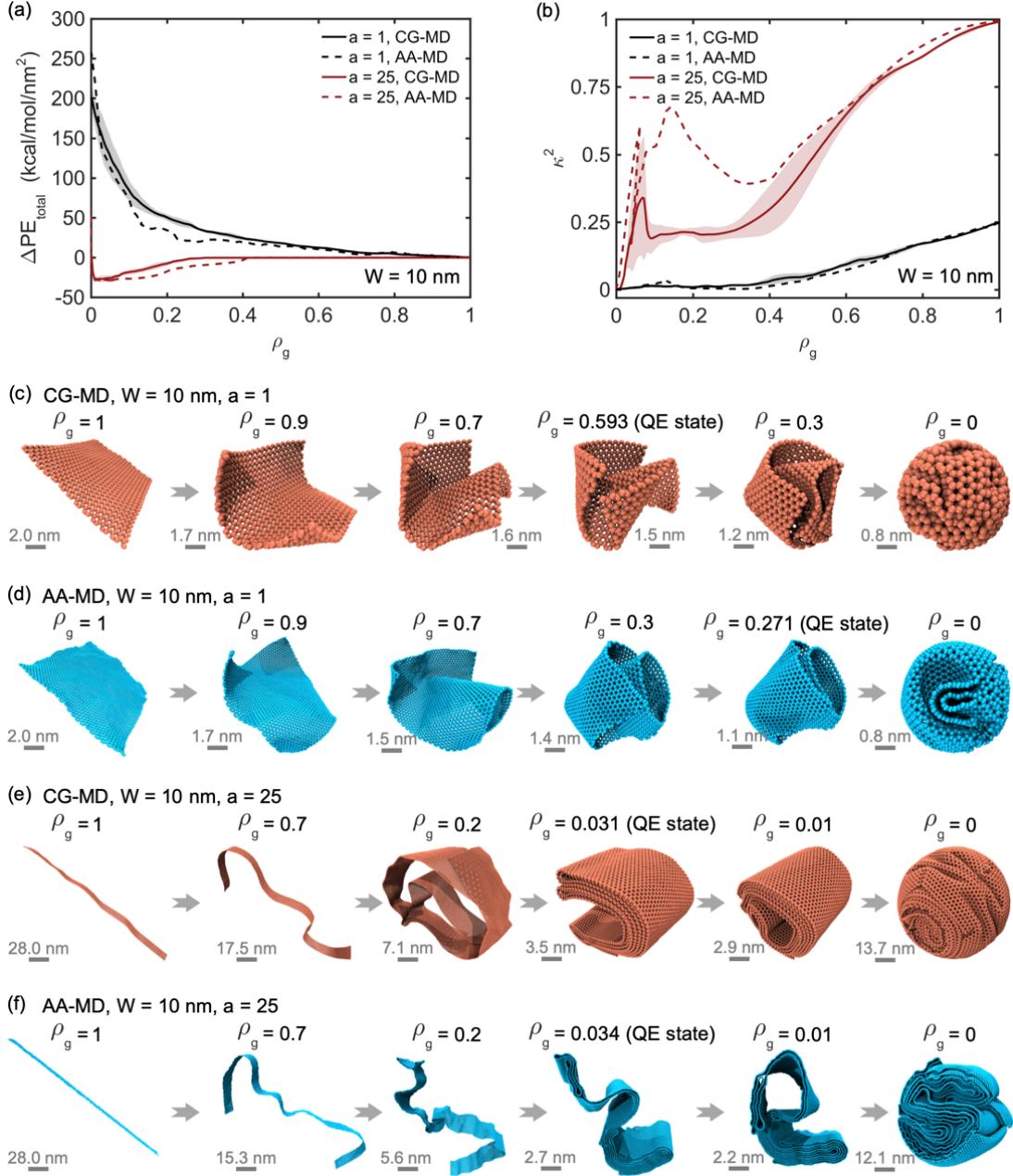


Fig. S4. Comparative analysis of coarse-grained (CG) and all-atom (AA) molecular dynamics (MD) simulations of the crumpling behavior for GNRs ($W = 10$) with $a = 1$ and 25, respectively. (a) Evolution of the total potential energy increment ΔPE_{total} as a function of the compaction ratio ρ_g in CG-MD and AA-MD simulations. (b) Evolution of relative shape anisotropy κ^2 with ρ_g in CG-MD and AA-MD simulations. Representative configurations of crumpled GNRs for different compaction ratios ranging from 0 to 1. (c) $a = 1$ in CG-MD simulation, (d) $a = 1$ in AA-MD simulation, (e) $a = 25$ in CG-MD simulation, (f) $a = 25$ in AA-MD simulation. Here, we conducted

a comparative analysis between coarse-grained molecular dynamics (CG-MD) and all-atom molecular dynamics (AA-MD) simulations for graphene nanoribbons (GNRs) with $W = 10$ nm and two representative aspect ratios: $a = 1$ and $a = 25$. Specifically, GNRs are simulated atomistically using the adaptive interatomic reactive empirical bond-order (AIREBO) potential for carbon-carbon interactions [1, 2]. The AIREBO potential has been shown to provide an accurate account of the chemical and mechanical behavior of hydrocarbons, including graphene [3, 4]. The rest of the system settings in the AA-MD simulation are consistent with CG-MD simulations. As shown in above figure, the evolution of the total potential energy increment (ΔPE_{total}) and the relative shape anisotropy (κ^2) during the crumpling process is highly consistent between CG-MD and AA-MD simulations. This indicates that the CG model employed in our study is capable of capturing the essential features of the crumpling dynamics. Furthermore, comparison of representative configurations at different compaction ratios confirms that the morphological characteristics observed in CG-MD closely match those in AA-MD. In particular, small GNRs exhibit edge-bending dominated (EBD) crumpling modes, while large GNRs favor sliding-and-folding dominated (SFD) modes, in agreement with the classification reported in our manuscript.

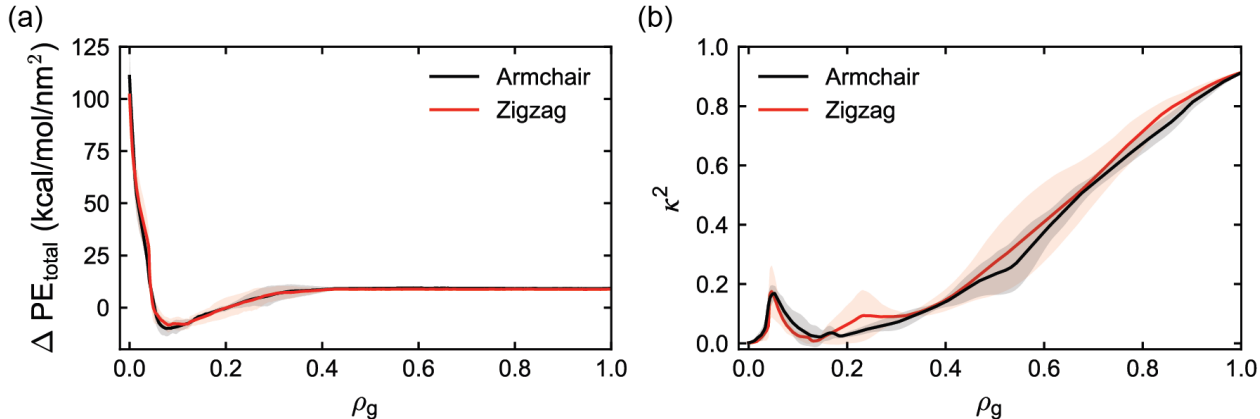


Fig. S5. Effect of chirality on the crumpling behavior of GNRs with $W = 10$ nm and $a = 6$. (a) Total potential energy increment ΔPE_{total} and (b) relative shape anisotropy κ^2 as a function of compaction ratio ρ_g for GNRs with zigzag and armchair edge configurations. Shaded areas correspond to the standard deviation. To examine the potential influence of edge chirality on the crumpling behavior of GNRs, we conducted additional simulations comparing nanoribbons with zigzag and armchair edge terminations, both having $W = 10$ nm and $a = 6$. As shown in above

figure, the evolutions of both the total potential energy increment (ΔPE_{total}) and the relative shape anisotropy (κ^2) exhibit close agreement between the two chiralities. The minor variations observed lie within the standard deviations obtained from independent runs, suggesting that edge chirality exerts a negligible influence on the overall crumpling pathway and final morphology under the current system size and isotropic compaction protocol. These results support our original assumption that the statistical features of crumpled morphologies are largely robust against symmetry-breaking effects introduced by edge orientation. That said, we acknowledge that for smaller systems, or in scenarios involving directional confinement or highly anisotropic environments, chirality may play a more pronounced role.

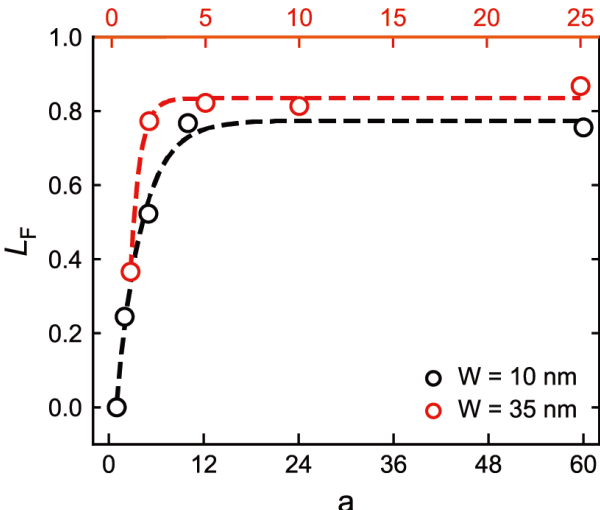


Fig. S6. The localization factor L_F of crumpled GNRs in the quasi-equilibrium (QE) state as a function of the aspect ratio a , for two different ribbon widths $W = 10$ nm and 35 nm. To better quantify the nature of surface contact and distinguish localized folding-induced interactions from global geometrical overlap, we adopt the localization factor L_F , which characterizes the degree of contact localization of the crumpled structure [5]. This metric has been used to differentiate short-range vs. long-range contact modes in confined or folded morphologies. As shown in above figure, L_F of GNRs in the QE state (Fig. 3(d) and (e) in the main manuscript) increases systematically with both aspect ratio a and ribbon width W , indicating that larger GNRs develop more localized and extensive contact regions during the crumpling process. Notably, L_F exhibits early saturation for large a , particularly in wide GNRs (e.g., $W = 35$ nm), suggesting that contact formation becomes more efficient as the sheet size increases. These results quantitatively support our

interpretation that the enhanced adhesion energy in larger GNRs is primarily due to genuine interfacial contact formation, rather than simple geometric proximity or overlap.

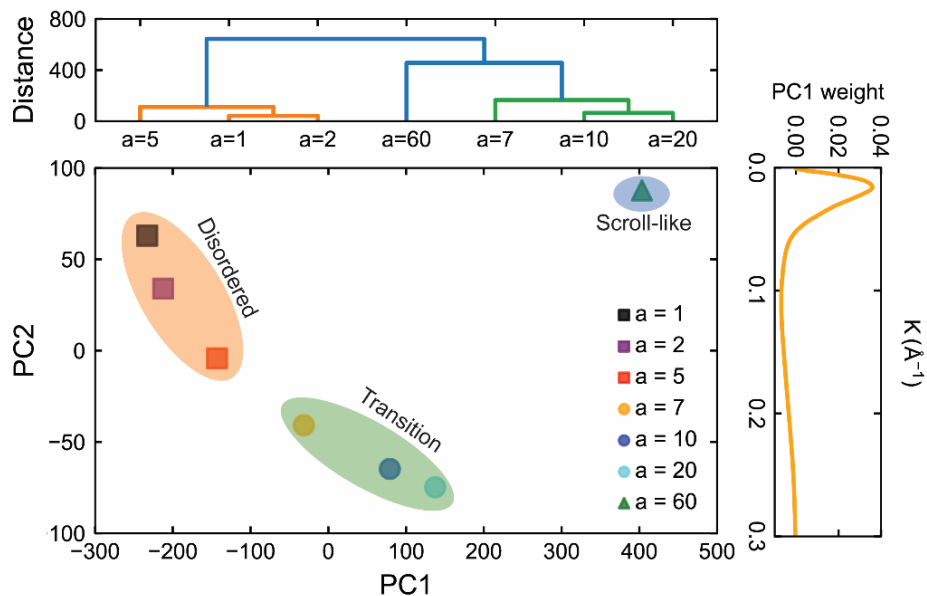


Fig. S7. Principal component analysis (PCA) of curvature-based features for crumpled GNRs with varying aspect ratios. The lower left panel shows the projection of samples in the PC1–PC2 space. The upper panel displays the corresponding hierarchical clustering dendrogram. The right panel shows the PC1 loading as a function of curvature K . PC1 and PC2 correspond to the first and second principal components obtained from the curvature probability distributions. To provide a more quantitative and objective classification, we have now performed principal component analysis (PCA) using the curvature probability distributions of crumpled GNRs as input features [6, 7]. As shown in above figure, the PCA projection onto the PC1–PC2 space reveals three clearly separated structural regimes (disordered, transitional, and scroll-like), which are further corroborated by hierarchical clustering analysis. The loading profile of PC1 indicates that low-curvature components contribute most significantly to the variance between different structures. This result is consistent with the curvature distributions shown in Fig. 6(b) in the main manuscript, where scroll-like structures (e.g., $a = 25$ and 60) exhibit sharp peaks centered at low curvature values, whereas disordered structures (e.g., $a = 1, 2, 5$) display broader distributions with higher curvature components. These analyses confirm that curvature-based PCA provides an effective

quantitative tool to distinguish between different crumpling modes in GNRs, complementing and validating our earlier qualitative observations.

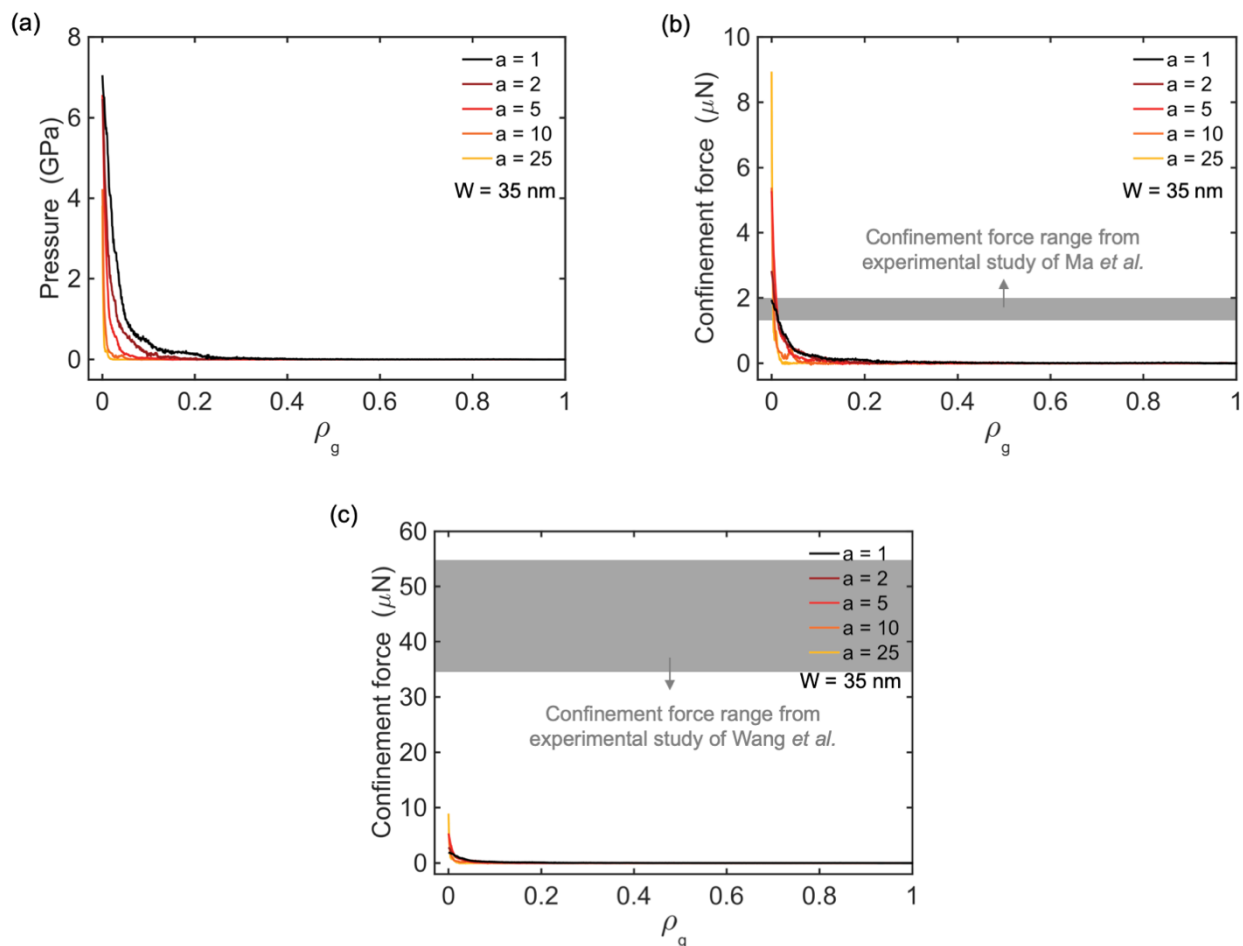


Fig. S8. Relationship between the pressure of the system with compaction ratio ρ_g during the crumpling process for GNRs ($W = 35$ nm) with aspect ratios a of 1, 2, 5, 10, and 25. (b) and (c). Relationship between the confinement force of the confining sphere on the GNR with ρ_g in the simulation. The gray shading in panels (b) and (c) highlights the range of confinement force for the crumpled graphene oxide system reported in the experimental work by Ma *et al.* [8] and Wang *et al.* [9], respectively. To further assess the feasibility of reaching the final crumpled (FC) state in our model, we analyzed the system pressure during the crumpling process and its relation to the compaction ratio ρ_g . As shown in Fig. S8(a), the pressure increases with compaction for GNRs of various aspect ratios ($a = 1$ to 25). This pressure was then converted into the confinement force

exerted by the spherical boundary, as shown in Fig. S8(b) and (c). Notably, for GNRs with a fixed width of $W = 35$ nm, the confinement force required to reach the FC state ranges from approximately $2 \mu\text{N}$ to $9 \mu\text{N}$ as the aspect ratio increases. These values are comparable in magnitude to those reported in aerosol evaporation-based experiments on crumpled graphene oxide: $1.6\text{--}2 \mu\text{N}$ (Ma *et al.* [8]) and $35\text{--}56 \mu\text{N}$ (Wang *et al.* [9]). Although our model represents an idealized process, the confinement force falls within a realistic experimental range, supporting the theoretical feasibility of the FC state. These results suggest that, under suitable experimental conditions, such crumpled conformations are in principle attainable.

References

- [1] Brenner, D. W., Shenderova, O. A., Harrison, J. A., Stuart, S. J., Ni, B., & Sinnott, S. B. (2002). A second-generation reactive empirical bondorder (REBO) potential energy expression for hydrocarbons. *Journal of Physics: Condensed Matter*, 14(4), 783.
- [2] Stuart, S. J., Tutein, A. B., & Harrison, J. A. (2000). A reactive potential for hydrocarbons with intermolecular interactions. *The Journal of Chemical Physics*, 112(14), 6472-6486.
- [3] Xu, Z., & Buehler, M. J. (2009). Strain controlled thermomutability of single-walled carbon nanotubes. *Nanotechnology*, 20(18), 185701.
- [4] Reddy, C. D., Ramasubramaniam, A., Shenoy, V. B., & Zhang, Y. W. (2009). Edge elastic properties of defect-free single-layer graphene sheets. *Applied Physics Letters*, 94(10), 101904.
- [5] Zhao, Y., Qin, J., Wang, S., & Xu, Z. (2022). Unraveling the morphological complexity of two-dimensional macromolecules. *Patterns*, 3(6), 100497.
- [6] Stein, S. A. M., Loccisano, A. E., Firestine, S. M., & Evanseck, J. D. (2006). Principal components analysis: a review of its application on molecular dynamics data. *Annual Reports in Computational Chemistry*, 2, 233-261.
- [7] Wold, S., Esbensen, K., & Geladi, P. (1987). Principal component analysis. *Chemometrics and Intelligent Laboratory Systems*, 2(1-3), 37-52.
- [8] Ma, X., Zachariah, M. R., & Zangmeister, C. D. (2012). Crumpled nanopaper from graphene oxide. *Nano letters*, 12(1), 486-489.
- [9] Wang, W. N., Jiang, Y., & Biswas, P. (2012). Evaporation-induced crumpling of graphene oxide nanosheets in aerosolized droplets: confinement force relationship. *The Journal of Physical Chemistry Letters*, 3(21), 3228-3233.